



1 **The important roles of surface tension and growth rate in**
2 **the contribution of new particle formation (NPF) to cloud**
3 **condensation nuclei (CCN) number concentration:**
4 **evidence from field measurements in southern China**

5 Mingfu Cai^{1,2,3,4}, Baoling Liang³, Qibin Sun³, Li Liu⁴, Bin Yuan^{1,2*}, Min Shao^{1,2}, Shan
6 Huang^{1,2}, Yuwen Peng^{1,2}, Zelong Wang^{1,2}, Haobo Tan⁴, Fei Li^{4,6}, Hanbin Xu³, and Jun
7 Zhao^{3,5,7*}

8 ¹ Institute for Environmental and Climate Research, Jinan University, Guangzhou, Guangdong 511443,
9 China

10 ² Guangdong-Hongkong-Macau Joint Laboratory of Collaborative Innovation for Environmental Quality,
11 Guangzhou, Guangdong 511443, China

12 ³ School of Atmospheric Sciences, Guangdong Province Key Laboratory for Climate Change and Natural
13 Disaster Studies, and Institute of Earth Climate and Environment System, Sun Yat-sen University,
14 Zhuhai, Guangdong 519082, China

15 ⁴ Institute of Tropical and Marine Meteorology/Guangdong Provincial Key Laboratory of Regional
16 Numerical Weather Prediction, CMA, Guangzhou 510640, China

17 ⁵ Southern Marine Science and Engineering Guangdong Laboratory (Zhuhai), Zhuhai, Guangdong
18 519082, China

19 ⁶ Laboratory of straits meteorology, Xiamen, Guangdong 361012, China

20 ⁷ Guangdong Provincial Observation and Research Station for Climate Environment and Air Quality
21 Change in the Pearl River Estuary, Guangzhou, Guangdong 510275, China

22

23 **Corresponding authors:* Bin Yuan (byuan@jnu.edu.cn) and Jun Zhao (zhaojun23@mail.sysu.edu.cn)

24



25 **Abstract.**

26 The contribution of new particle formation (NPF) to cloud condensation nuclei (CCN) number
27 concentration varies largely under different environments, depending on several key factors such as
28 formation rate (J), growth rate (GR), distribution of preexisting particles and properties of new particles
29 during NPF events. This study investigated the contribution of NPF to the N_{CCN} and its controlling factors
30 based on measurements conducted at the Heshan supersite, in the Pearl River Delta (PRD) region of
31 China during fall-time 2019. The size-resolved cloud condensation nuclei activity and size-resolved
32 particle hygroscopicity were measured by a cloud condensation nuclei counter (CCNc) and a hygroscopic
33 tandem differential mobility analyzer (HTDMA), respectively, along with a scanning mobility particle
34 sizer (SMPS) and a diethylene glycol scanning mobility particle sizer (DEG-SMPS) for particle number
35 size distribution (PNSD). A typical NPF event on 29th October was chosen to investigate the contribution
36 of the NPF to N_{CCN} under several supersaturation ratios. Two particle properties (hygroscopicity and
37 surface tension) affect CCN activation with the latter being more important in terms of the CCN
38 concentration (N_{CCN}). A lower value of surface tension (i.e., 0.06 N m^{-1}) than pure water assumption
39 (0.073 N m^{-1}) could increase the N_{CCN} at $SS=1.0\%$ by about 20% during non-event period and by about
40 40% during the event. In addition, an earlier peak time corresponding to a lower critical diameter (D_{50})
41 was also observed. The results show that high formation rate, growth rate, and low background particle
42 concentration lead to high number concentrations of newly-formed particles. The high growth rate was
43 found to have the most profound impact on the N_{CCN} which can be attributed to the facts that a higher
44 growth rate can grow particles to the CCN size in a shorter time before they are scavenged by pre-existing
45 particles. Two other NPF events (an event on 18th October in this campaign and an event on 12th
46 December, 2014 in Panyu) were chosen to perform sensitivity tests under different scenarios (growth



47 rate, formation rate, and background particle concentration). The calculated N_{CCN} at $SS=1.0\%$ on 12th
48 December, 2014 was significantly lower than that from the other two events. The event on 12th December
49 was re-simulated using high growth rate taken from the event on 18th October which resulted in similar
50 CCN concentrations between the two events (12th December and 18th October), implying that the growth
51 rate is the most controlling factor for CCN activation. Our results highlight the importance of growth rate
52 and surface tension when evaluating the contribution of NPF to the N_{CCN} .

53 **1 Introduction**

54 Atmospheric particles have direct effects on global climate by adsorbing and scattering solar
55 radiation, while they can act as cloud condensation nuclei (CCN) and exert influences on cloud formation,
56 life cycle, and albedo, hence indirectly affect the global radiation balance. In general, atmospheric
57 particles have a cooling effect on the global climate, although the highest uncertainty exists on their
58 climatic contribution among all the climatic forcings (Stocker et al., 2013). The relationship between the
59 CCN number concentration (N_{CCN}) and its climatic effect represents one of the major uncertainties and
60 challenges in evaluating the aerosol climatic effect. It is hence essential to carry out field measurements
61 to investigate the CCN activity and its controlling factors.

62 New particle formation (NPF) as an important source of global atmospheric particles, is frequently
63 observed in various atmospheric environments, including forest, urban, and agricultural regions
64 (Kulmala et al., 2004). Once formed, the particles can grow to the CCN sizes (50-100 nm) within a few
65 hours and contribute significantly to the N_{CCN} (Leng et al., 2014; Spracklen et al., 2008; Dameto de
66 España et al., 2017). The extent to which newly-formed particles can contribute to the N_{CCN} is controlled
67 by many factors, including formation rate (J), growth rate (GR), background particle number size



68 distribution (PNSD), and properties of the particles. The formation rate is defined as a flux of newly-
69 formed particles at a threshold diameter and is usually used to describe how many particles are produced
70 into the atmosphere during an event. The growth rate (GR) represents the diameter change of the particles
71 in a certain time period, and particles with a higher GR will grow to the CCN sizes in a shorter time. The
72 background PNSD controls the scavenging of the newly-formed particles, and the high concentration of
73 pre-existing particles will efficiently scavenge these particles before they can grow to the CCN sizes.
74 The properties of the particles (e.g., chemical composition, hygroscopicity, and surface tension) affect
75 their ability of acting as CCN. In general, particles containing a higher fraction of inorganic matters or
76 water-soluble organics are more hygroscopic and are more easily activated due to a lower critical
77 diameter (D_{50}). Recent studies showed that surfactant effects of organic matters were found on the
78 particle surface which could lead to an increase of the CCN activity (Ovadnevaite et al., 2017; Cai et al.,
79 2018; Liu et al., 2018). The contribution of NPF to N_{CCN} is difficult to be quantitatively evaluated and
80 currently the controlling factors are not fully understood, constraining an accurate quantification of the
81 aerosol climatic forcing from NPF.

82 NPF event was well known to have an important contribution to the N_{CCN} , while a wide range of
83 N_{CCN} during NPF events was reported in the literature. Yue et al. (2011) showed that the N_{CCN} during
84 NPF events was increased by a factor of 0.4-6 in Beijing. However, much less (a factor of 1.17-1.88)
85 increase of the N_{CCN} was observed during NPF events in Shanghai (Leng et al., 2014). The results from
86 Ma et al. (2016) showed that the N_{CCN} was significantly impacted by the hygroscopicity of newly-formed
87 particles during NPF events in the North China Plain (NCP). Yu et al. (2014) reported an average factor
88 of 4.7 increase of the N_{CCN} during NPF events from growth of new particles to the CCN sizes in Ozark
89 forest. Rose et al. (2016) showed that NPF could be a larger contributor to N_{CCN} compared to transport



90 in free troposphere. A long-term field measurement in the urban Vienna conducted by Dameto de España
91 et al. (2017) reported that the N_{CCN} (at 0.5% ss) could increase up to 143% during NPF events.
92 Kalkavouras et al. (2017) found that the NPF could double the N_{CCN} (at 0.1% ss), but could augment the
93 potential droplet number only by 12%.

94 Factors that control the CCN activity of newly-formed particles (formation rate, growth rate, and
95 particle properties) were investigated worldwide. These parameters varied substantially in a large
96 temporal and spatial scale. For example, the mean formation rate of 10 nm particles (J_{10}) was 3.7 cm^{-3}
97 s^{-1} in Nanjing (An et al., 2015), which was much higher than that ($0.40 \text{ cm}^{-3} \text{ s}^{-1}$) reported in Shanghai
98 (Leng et al., 2014). A value of $3.3\text{--}81.4 \text{ cm}^{-3} \text{ s}^{-1}$ was reported for the mean formation rate of 3 nm particles
99 (J_3) based on one-year long measurements in Beijing (Wu et al., 2007). In the NCP region, a long-term
100 measurement conducted by Shen et al. (2011) reported that the J_3 ranged from 0.7 to $72.7 \text{ cm}^{-3} \text{ s}^{-1}$, with
101 a mean value of $8.0 \text{ cm}^{-3} \text{ s}^{-1}$. Shen et al. (2019) reported an average J_3 value of $1.30 \text{ cm}^{-3} \text{ s}^{-1}$ at Mountain
102 Tai, which was much lower than urban regions. The growth of newly-formed particles can be
103 characterized by the particle growth rate. Kulmala et al. (2004) summarized a wide range of growth rate
104 (1 to 20 nm h^{-1}) from more than 100 field measurements of NPF in mid-latitudes. On the one hand, the
105 growth rates are usually high in polluted region, for example, a growth rate of $11.6\text{--}18.1 \text{ nm h}^{-1}$ was
106 reported in New Delhi, India (Kulmala et al., 2005; Mönkkönen et al., 2005). On the other hand, the
107 growth rates are in general low in forest regions, for example, a median value of 2.5 nm h^{-1} was reported
108 from long term measurements (Nieminen et al., 2014). Furthermore, large uncertainties exist for the
109 measured growth rates even in the same region. For example, the growth rates under sulfur-poor
110 conditions were about 80% higher than those under sulfur-rich conditions in Beijing (Yue et al., 2011).
111 The condensable vapors not only control the growth rate, but also decide the hygroscopicity of newly-



112 formed particle, which can vary in a large range from event to event. Wu et al. (2013a) reported a
113 hygroscopic growth factor of 1.2 to 1.55 during NPF events in a mountain region, Germany. Asmi et al.
114 (2010) found a significant contribution of organic vapors to particle formation and growth, leading to a
115 low hygroscopicity of newly-formed particles in the Antarctica region. The above studies show large
116 temporal and spatial variations of characteristics in the properties of newly-formed particles (i.e., the
117 formation rate, growth rate and hygroscopicity) during NPF events. However, how these parameters
118 contribute to the variation of the N_{CCN} during NPF events in various regions is yet to be investigated.

119 Although the Pearl River Delta region (PRD), one of the most economically developed areas in
120 China, has made substantial progress in mitigating haze pollution, especially in achieving $PM_{2.5}$ national
121 level II standard (an average annual mass concentration of less than $35 \mu\text{g m}^{-3}$ for $PM_{2.5}$), the intensive
122 human activities and photochemistry lead to emissions and productions of a large amount of condensable
123 air pollutants for initiating formation of atmospheric particles and promoting their subsequent growth.
124 Several studies reported the frequent occurrences of NPF events in urban and rural areas of the PRD
125 which provide a large amount of particles to the local atmosphere (Yue et al., 2013; Liu et al., 2008; Yue
126 et al., 2016; Wang et al., 2013). However, these studies focused primarily on the characteristics of the
127 NPF events, the contribution to the N_{CCN} and the controlling factors were still unknown, hindering an
128 accurate assessment of NPF in CCN formation and eventually global climate change.

129 In this study, we analyzed the contribution of NPF to the N_{CCN} based on a rural field campaign
130 conducted at the Heshan supersite in the PRD region during Fall (October and November, 2019). A suite
131 of advanced analytical instruments were employed to measure particle hygroscopicity, size-resolved
132 CCN activity, and particle number size distribution (1 nm - 10 μm). Here, we select three representative
133 NPF events (two from this measurement, the other one from a previous measurement in Panyu,



134 Guangzhou, 2014) to quantitatively investigate the contribution of NPF to the N_{CCN} and impact factors (i.e.,
135 formation rate, growth rate, background particle concentration, and particle properties) that manipulate
136 the contribution.

137 **2 Measurement site, instrumentation, and methodology**

138 **2.1 Measurement site**

139 The field campaign was conducted at the Heshan supersite in the Guangdong Province of China
140 during the Fall season (from 27th September to 17th November, 2019). This rural site (22°42'39. 1"N,
141 112°55'35.9"E) is located at the southwest of the PRD region (about 70 km away from megacity
142 Guangzhou) with an altitude of about 40 m above sea-level and the site is surrounded by several farms
143 and villages. All the instruments were placed in an air-conditioned room (T=298K) on the top floor of
144 the building at the supersite, administrated by Guangdong Provincial Environmental Monitoring Centre.
145 An aerosol sampling port equipped with a PM₁₀ cyclone inlet was made of a 6 m long 3/8" o.d. stainless-
146 steel tube. The sampling air was dried to a relative humidity (RH) lower than 30% by passing through a
147 Nafion dryer (model MD-700, Perma Pure, Inc., USA) before the air entered into the individual
148 instruments.

149 **2.2 Instrumentation**

150 **2.2.1 Particle number size distribution and size-resolved CCN activity measurements**

151 The particle number size distribution (PNSD) in a complete size range of 1 nm- 10 μ m (an upper
152 cut size of 10 μ m) was measured by a diethylene glycol scanning mobility particle sizer (DEG-SMPS,



153 model 3938E77, TSI Inc., USA), a SMPS (model 3938L75, TSI Inc., USA), and an aerodynamic particle
154 sizer (APS, model 3321, TSI Inc., USA). The DEG-SMPS was applied to measure particles with a size
155 range of 1-30 nm, consisted of a nano-differential mobility analyzer (nDMA, model 3086, TSI Inc., USA),
156 a nano enhancer (model 3777, TSI Inc., USA), and a condensation particle counter (CPC, model 3772,
157 TSI Inc., USA). The SMPS composed of a DMA (model 3081A, TSI Inc., USA) and a CPC (model 3775,
158 TSI Inc., USA) was employed to measure particles in a size range of 10-800 nm. The APS was used to
159 measured submicron particles ranging from 0.5 μm to 10 μm .

160 Size-resolved CCN activity was measured with a combination of a cloud condensation nuclei
161 counter (CCNc, model 200, DMT Inc., USA) and another SMPS. The CCNc-200 has two parallel cloud
162 columns, which can be used to measure the CCN concentration (N_{CCN}) simultaneously. The
163 supersaturation of each column was set to be 0.1%, 0.2% and, 0.4%, 0.7%, 0.9%, and 1.0%, respectively.
164 The dry particles were firstly neutralized by an X-ray neutralizer (model 3088, TSI Inc., USA) and were
165 then classified by a DMA (model 3081A, TSI Inc., USA). The monodisperse particles were split into
166 three streams: two to the CCNc for measurement of the N_{CCN} (with a flow rate of 0.6 LPM) and one to
167 the CPC for measurement of total particle number concentration (N_{CN} , with a flow rate of 0.3 LPM).
168 Prior to the campaign, the SMPSs was calibrated with standard polystyrene latex spheres (PSL, with a
169 size of 20, 50, and 200 nm) and the CCNc-200 was calibrated with ammonium sulfate $((\text{NH}_4)_2\text{SO}_4$
170 particles at the six SSs (0.1%, 0.2%, 0.4%, 0.7%, 0.9%, and 1.0%).

171 2.2.2 Aerosol hygroscopicity measurement

172 Hygroscopicity of atmospheric particle at various size ranges was measured by a hygroscopic
173 tandem differential mobility analyzer (HTDMA), consisted of two DMA (model 3081L, TSI Inc., USA),



174 a Nafion humidifier (model MD-700, Perma Pure Inc., USA), a heated tube and a condensation particle
175 counter (model 3788, TSI Inc., USA). The dry particles were firstly neutralizer by an X-ray neutralizer
176 (model 3088, TSI Inc., USA) and subsequently were classified by a DMA for six sizes in this study (30,
177 50, 80, 100, 150, and 200 nm). The selected particles at a specific diameter (D_0) were then introduced
178 into a humidifier under a fixed RH (90% in this study). Another DMA and a CPC were used to measure
179 size distribution of humidified particles (D_{wet}).

180 2.3 Methodology

181 2.3.1 Estimation of hygroscopicity based on the measurements

182 The size-resolved activation ratio (AR) could be obtained from the measured N_{CN} and N_{CCN} by the
183 SMPS and CCNc-200 system and was inverted based on the method described by Moore et al. (2010).

184 The AR was then fitted with the sigmoidal function with respect to particle diameter D_p ,

$$185 \frac{N_{CCN}}{N_{CN}} = \frac{B}{1 + (\frac{D_p}{D_{50}})^C} \quad (1)$$

186 where B , C , and D_{50} are fitting coefficients. The D_{50} represents the critical diameter at which half of
187 the particles are activated at a specific SS.

188 The hygroscopic parameter κ can be obtained from the critical supersaturation (S_c) and the D_{50}
189 (Petters and Kreidenweis, 2007) by

$$190 \kappa = \frac{4A^3}{27D_{50}^3(\ln S_c)^2}, \text{ where } A = \frac{4\sigma_{s/a}M_w}{RT\rho_w} \quad (2)$$

191 where $\sigma_{s/a}$ is the surface tension of the solution/air interface and here it is temporarily assumed to be that
192 of pure water (0.0728 N m⁻¹ at 298.15 K), M_w is the molecular weight of water (0.018 kg mol⁻¹), R is
193 the universal gas constant (8.31 J mol⁻¹ K⁻¹), T is the thermodynamic temperature in Kelvin (298.15 K),



194 and ρ_w is the density of water (about 997.04 kg m^{-3} at 298.15 K).

195 The growth factor (GF) of selected particles can be calculated according to the following equation,

$$196 \quad Gf = \frac{D_{wet}}{D_0} \quad (3)$$

197 In addition to the hygroscopic parameter calculated based on the SMPS and CCNc-200 system, the κ can
198 also be calculated from HTDMA measurement based on the growth factor,

$$199 \quad \kappa = (Gf^3 - 1) \left[\frac{1}{RH} \exp \left(\frac{A\sigma_s/aM_w}{RT\rho_w D_0} - 1 \right) \right] \quad (4)$$

200 Due to the effect of DMA diffusing transfer function, the TDMAfit algorithm (Stolzenburg and McMurry,
201 2008) was applied to narrow the uncertainty and fit the growth factor probability density function (GF-
202 PDF). Detailed data inversion process can be found elsewhere in Tan et al. (2013).

203

204 2.3.2 Estimation of H_2SO_4 concentration and its contribution to particle growth

205 The daytime gas phase H_2SO_4 concentration is estimated according to the proxy presented by Petäjä
206 et al. (2009),

$$207 \quad [\text{H}_2\text{SO}_4] = \frac{k \cdot [\text{SO}_2] \cdot [\text{OH}]}{CS} \quad (5)$$

208 where k is the reaction rate constant and is assumed to be $8.5 \times 10^{-13} \text{ cm}^3 \text{ molecule}^{-1} \text{ s}^{-1}$ in this study
209 (Chen et al., 2014; Wang et al., 1988; Vignati et al., 2004), $[\text{SO}_2]$ is the concentration of SO_2 in molecules
210 cm^{-3} , $[\text{OH}]$ is the concentration of OH radical in molecules cm^{-3} , and the CS is the condensation sink in
211 s^{-1} and it can be calculated from following equation,

$$212 \quad CS = 2\pi D \sum_{Dp_i=Dp_{min}}^{+\infty} \beta_{m,i} N_i \quad (6)$$

213 where D is the diffusion coefficient of the H_2SO_4 vapor (assumed to be $0.8 \times 10^{-5} \text{ m}^2 \text{ s}^{-1}$ in this study),

214 $\beta_{m,i}$ is the transitional regime correction factor which can be calculated from the Knudsen number



215 (Fuchs and Sutugin, 1971), and N_i represents the particle number concentration at $D_{p,i}$.

216 Framework for 0-D Atmospheric Modeling (F0AM) v3.1 (Wolfe et al., 2016) is a zero-dimensional
217 atmospheric box model which was used to simulate the concentration of OH radical in the atmosphere.
218 The model was constrained with a set of online measured trace gases, VOCs, and meteorological data.
219 The employed chemical mechanism is Master Chemical Mechanism (MCM) v3.3.1. More detailed
220 description of model setup can be found in Wang et al. (2020).

221 The required vapor concentration of H_2SO_4 ($C_{v,GR=1\text{ nm h}^{-1}}$) for a growth rate of 1 nm h^{-1} in a
222 certain particle size range ($D_{p,initial}$ to $D_{p,final}$) can be calculated from the following equation,

$$223 \quad C_{v,GR=1\text{ nm h}^{-1}} = \frac{2\rho_v d_v}{\alpha_m m_v \Delta t} \cdot \sqrt{\frac{\pi m_v}{8kT}} \cdot \left[\frac{2x_1+1}{x_1(x_1+1)} - \frac{2x_0+1}{x_0(x_0+1)} + 2\ln\left(\frac{x_1(x_0+1)}{x_0(x_1+1)}\right) \right] \quad (8)$$

224 where ρ_v , m_v and D_v is the density, mass and diameter of H_2SO_4 , which was assumed to be 1830 kg
225 m^{-3} , 98 amu , and 0.55 nm , respectively (Nieminen et al., 2010; Jiang et al., 2011), α_m is the mass
226 accommodation coefficient (assumed to be unity in this study), x_1 and x_0 are the ratios of D_v to
227 $D_{p,final}$ (10 nm in this study) and $D_{p,initial}$ (3 nm in this study), Δt (in s) is the time for particle growth
228 from $d_{p,initial}$ to $d_{p,final}$ ($\Delta t = \frac{d_{p,final} - d_{p,initial}}{GR}$) with a growth rate of 1 nm h^{-1} , and k is the
229 Boltzmann constant ($1.38 \times 10^{23}\text{ J K}^{-1}$).

230 Thus, the growth rate contributed from condensation of H_2SO_4 vapor can be obtained,

$$231 \quad GR_{H_2SO_4} = \frac{[H_2SO_4]}{C_{v,GR=1\text{ nm h}^{-1}}} \quad (9)$$

232 The average calculated H_2SO_4 concentration during particle growth can be calculated using Eq. (5). The
233 resultant $GR_{H_2SO_4}$ can be overestimated because the assumption of unity for α_m in Eq. (8) is not
234 necessary the case because not all H_2SO_4 molecules end up loss for their collisions with pre-existing
235 particles.



236 2.3.3 Estimation of growth rate (GR) and formation rate (J)

237 The observed particle growth rate (GR) is defined as the diameter change of nucleated particles
 238 (dDp_{nuc}) for a time period (dt),

$$239 \quad GR = \frac{dDp_{nuc}}{dt} \quad (10)$$

240 Here log-normal distribution function method was adopted and the PNSD was fitted to obtain the
 241 representative diameter for nucleated particles during NPF events (Kulmala et al., 2012),

$$242 \quad \frac{dN}{d \log D_p} = \frac{N}{\sqrt{2\pi}\sigma} \exp\left(-\frac{\ln^2\left(\frac{D_p}{Dp_{gmd}}\right)}{2\sigma^2}\right) \quad (11)$$

243 where D_p is particle diameter, N is total particle number concentration, Dp_{gmd} is geometric mean
 244 particle diameter and it was also used as the representative particle size in Eq. (10). In this study, the
 245 PNSD was found to have a significant mode in a size range of 3- 60 nm during NPF events and we hence
 246 applied one log-normal mode fitting. At each time step, the PNSD was fitted using Eq. (11) and the
 247 Dp_{gmd} as a function of time, that is, the growth rate, was determined according to Eq. (10).

248 The formation rate (J_k) described the flux through a certain diameter (k) during NPF events and it
 249 is calculated based on the formula given in Cai and Jiang (2017),

$$250 \quad J_k = \frac{dN_{[Dp_k, Dp_u]}}{dt} + \sum_{Dp_g=Dp_k}^{Dp_u-1} \sum_{Dp_i=Dp_{min}}^{+\infty} \beta_{(i,g)} N_{[Dp_i, Dp_{i+1}]} N_{[Dp_g, Dp_{g+1}]} -$$

$$251 \quad \frac{1}{2} \sum_{Dp_g=Dp_{min}}^{Dp_u-1} \sum_{Dp_i^2=\max(Dp_{min}^3, Dp_k^3-Dp_{min}^3)}^{Dp_{i+1}^3+Dp_{g+1}^3 \leq Dp_u^3} \beta_{(i,g)} N_{[Dp_i, Dp_{i+1}]} N_{[Dp_g, Dp_{g+1}]} + n_u \cdot GR_u \quad (12)$$

252 where $N_{[Dp_k, Dp_u]}$ is particle number concentration in a size range from Dp_k to Dp_u (exclude particles
 253 with diameter Dp_u), Dp_k and Dp_u are the lower and upper bound diameters (here 3 and 30 nm
 254 respectively), $\beta_{(i,g)}$ is the coagulation coefficient for collisions between particles with diameter Dp_i
 255 and particles with diameter Dp_g , n_u is the particle distribution function at Dp_u and GR_u is the
 256 growth rate calculated using Eq. (10) at Dp_u . Note that the calculation of formation rate using Eq. (12)



257 is based on two assumptions: (1) Dilution and other particles sources and losses except for coagulation
258 loss in the size range from Dp_k to Dp_u are negligible; (2) Net coagulation of particles is negligible.

259 2.3.4 Measurement based NPF simulations

260 For a regional NPF event, the evolution of particle size distribution is governed by the population
261 balance equations (Lehtinen et al., 2003; Kuang et al., 2012):

$$262 \quad \frac{dN_{k^*}}{dt} = J_{k^*} - GR \cdot n_{k^*} - N_{k^*} \sum_{Dp_i=Dp_{min}}^{+\infty} \beta_{(k^*,i)} N_i \quad (13-1)$$

$$263 \quad \frac{dN_k}{dt} = GR \cdot n_{k-1} - GR \cdot n_k + \frac{1}{2} \sum_{Dp_i=Dp_{min}}^{k-1} \beta_{(i,\varphi)} N_i N_\varphi - N_k \sum_{Dp_i=Dp_{min}}^{+\infty} \beta_{(k,i)} N_i \quad (13-2)$$

$$264 \quad Dp_\varphi^3 = Dp_k^3 - Dp_i^3 \quad (13-3)$$

265 In the equations, class k^* represents the smallest stable particle (here 3 nm particles), J_{k^*} is the
266 formation rate calculated using Eq. (12). Class k represents the particles with diameter Dp_k . The first,
267 second, and third terms on the right-hand side (RHS) of Eq. (13-1) represent the formation, condensation,
268 the coagulation sink terms, respectively. The first and second terms, the third, and fourth terms on the
269 RHS of Eq. (13-2) represent the condensation growth terms, a coagulation source (CoagSrc) term, and
270 the coagulation sink (CoagSnk) term, respectively.

271 For a specific NPF event, the evolution of PNSD with a size range of 3-1000 nm was simulated
272 based on Eq. (13) using Matlab (version 2016a, Mathworks, Inc.). In the simulation, the background
273 particle distribution was assumed to be the average PNSD before 6:00 LT, the growth rate and formation
274 rate were the measured values obtained from Eq. (10) and Eq. (13), respectively, and the time step was
275 set to be 10s. The simulation is based on following assumptions: (1) The dynamics of newly-formed
276 particles are driven by coagulation and condensation. The influences of transportation, primary emissions,
277 dilution, and particle evaporation are negligible. (2) The influence of coagulation on the preexisting



278 particles is negligible. (3) The particle growth rate for all particle sizes is assumed to be the same at a
279 time during NPF events.

280 3 Results and discussion

281 3.1 New Particle Formation (NPF) events at the Heshan Site

282 A total of 20 NPF events were observed during this seven-weeks long field campaign. Here we
283 selected a typical event (29th October, 2019) for further investigation. As shown in Fig. 1a, new particle
284 formation occurred at about 9:50 Local Time (LT) when a significant concentration of 3-10 nm particles
285 were observed. Subsequently, continuous and steady growth of the newly-formed particles was observed
286 until the particles grew to about 70-80 nm at about 20:00 LT. The blue dots in Fig. 1a represent the Dp_{gmd}
287 of nucleated particles and the red line represents the linear fitting, leading to an estimated growth rate of
288 8.0 nm h^{-1} . Prior to the event (around 9:50), the total particle number concentration (N_{CN}) remained low
289 (a concentration slightly below 10000 cm^{-3}) and rapidly increased when NPF event occurred, and then
290 reached its peak (about 56000 cm^{-3}) at 11:15 LT and subsequently decreased to 20000 cm^{-3} at about 15:00
291 LT, and remained at this concentration for the rest of the day. A steady north wind was observed before
292 18:00 LT and shifted to northwest afterwards (Fig. 1c). The shift of wind direction led to change of air
293 mass as seen from the PNSD, leading to a sudden increase of the N_{CN} at 18:00 LT (Fig. 1a and b). The
294 CCN concentration (N_{CCN}) at 1.0% SS increased from 5000 cm^{-3} at around 10:00 to 11000 cm^{-3} at about
295 15:00 LT, when the nucleated particles grew to the CCN size (Fig. S1). The D_{50} at 1.0% SS was apparently
296 the smallest critical diameters among all the SSs, the size that was easily reached during NPF and was
297 significantly affected by the newly-formed particles, we thus only discussed the variation of the N_{CCN} at



298 1.0% SS in the following section. The sudden increase of N_{CCN} at 18:00 LT could be attributed to change
299 of the air mass due to transportation, consistent with the changes of the PNSD, the N_{CN} , and wind
300 direction (Fig. 1a-c). The activation ratio (AR) was about 0.5 before dawn and dropped to about 0.2 just
301 prior to the event (Fig. 1b). This ratio continued to decrease to its trough at the time corresponding to the
302 maximum of N_{CN} and then increased again to about 0.6 at 15:00 LT during particle growth, slightly higher
303 than the value before dawn. Clearly, NPF can not only add a large number of particles to the atmosphere
304 but also increase the N_{CCN} and AR after particles are formed and grow. The wind speeds were about 3 m
305 s^{-1} during initial formation and growth, and decreased to about 1.5 $m s^{-1}$ during most of the particle
306 growth periods.

307 Formation of gaseous H_2SO_4 was favored by intensive photochemistry. Significant j -values of $O(^1D)$
308 (in s^{-1}) were observed during the day (from about 7:00 to 17:00) with a maximum value of $2 \times 10^{-5} s^{-1}$ at
309 noon and symmetrically distributed before and after noon. The average calculated concentration of
310 H_2SO_4 during particle formation (10:00-12:00 LT) was about $1.9 \times 10^7 cm^{-3}$, about an order higher than
311 that (about $7 - 12 \times 10^6 cm^{-3}$) in a mountain region in Germany (Wu et al., 2013a) and close to that (about
312 $2-5 \times 10^7 cm^{-3}$) in a rural region of Sichuan in China (Chen et al., 2014). Considering an uncertainty of
313 40% in estimation of H_2SO_4 concentration (Wu et al., 2013b), the GR contributed by condensation of
314 gaseous H_2SO_4 only was about 0.78-1.12 $nm h^{-1}$, or about 5.6% -20.0% of the total observed particle
315 growth rate in a size range of 3-10 nm. This implies that other compounds (e.g., organic vapors) than
316 H_2SO_4 play significant roles in the growth process of newly-formed particles which was widely reported
317 in literatures (Boy et al., 2005; Casquero-Vera et al., 2020; Paasonen et al., 2010).



318 **3.2 The impact of hygroscopicity and surfactants on κ_{CCN}**

319 The ability that atmospheric particles can serve as CCN is determined by several factors including
320 sizes, chemical composition, surface tension, and water saturation ratio of the particles (Farmer et al.,
321 2015). The organic matter in particles can act as surfactants to lower the surface tension of the particles
322 and hence can increase the CCN activity (Ovadnevaite et al., 2017). Previous studies showed that the
323 presence of surfactants led to discrepancies of κ values between measurements using different techniques
324 under sub-saturation (HTDMA measurements) or supersaturation conditions (κ_{CCN} measurements) (Cai
325 et al., 2018; Wex et al., 2009; Rastak et al., 2017). Figure 2 compares the κ values measured from several
326 locations including Heshan (this study, rural), Panyu (urban PRD, Cai et al., 2018, 2019), and South
327 China Sea (Cai et al., 2020). The median κ values measured by HTDMA in this study ranged from 0.1
328 to 0.18 in a size range of 30-200 nm, similar to those of particles primarily composed of organics (Deng
329 et al., 2018; Liu et al., 2018; Pajunoja et al., 2015), implying that chemical composition of the measured
330 particles was dominated by organics. In particular, the κ values measured using HTDMA (κ_{HTDMA}) in this
331 study were significantly lower than those from other studies. The κ values in a range of 0.21-0.31 were
332 reported for urban PRD and suburban North China Plain, which were likely attributed to high fractions
333 of water-soluble organic matters and inorganic compounds from traffic and industry emissions. The κ
334 values measured using κ_{CCN} fall in a range from 0.19 to 0.46, much higher than those from
335 measurements using HTDMA in this study. The discrepancy of the κ_{HTDMA} and κ_{CCN} values suggests
336 that surfactant effects could play an important role in CCN activation under sub-saturation and
337 supersaturation environments. Previous studies have shown that the organics in particles could lower
338 surface tension by about 0.01-0.032 N m⁻¹ (Ovadnevaite et al., 2017; Liu et al., 2018; Engelhart et al.,



339 2008; Cai et al., 2018), leading to the decrease of the D_{50} and higher κ values.

340 A new surface tension ($\sigma_{s/a}^*=0.060 \text{ N m}^{-1}$) was adopted to calculate the κ_{CCN} using Eq. (2) based on
341 the measured critical diameter (D_{50}), which brought the κ_{CCN} values at SS=1.0% and 0.9% within those
342 of KHTDMA, although the κ_{CCN} values with this new $\sigma_{s/a}^*$ at other SSs were still higher, implying that the
343 surface tension is dependent on particle diameter. Surfactants can lower the D_{50} of the particle which
344 then facilitates its activation as CCN. For particles with the same κ value, the measured D_{50} by fitting of
345 N_{CCN}/N_{CN} using Eq. (1) was lower than the calculated value based on pure water surface tension using
346 Eq. (2) due to the surfactant effect. In order to estimate the impact of surfactant on particle activation,
347 the D_{50} was recalculated using the surface tension of pure water (0.072 N m^{-1}) by Eq. (2) based on the κ
348 value from the CCN measurements with a surface tension correction (refer to κ_{CCN} , $\sigma_{s/a}^*$ and $\sigma_{s/a}^*=0.060$
349 N m^{-1} in Fig. 2). We termed the above recalculated D_{50} as the $D_{50, \sigma_{s/a}}$ to illustrate the surfactant effects
350 on the CCN activity during NPF events. Figure 3 shows the variation of the recalculated D_{50} (here
351 $\sigma_{s/a}=0.072 \text{ N m}^{-1}$) and the measured D_{50} , along with the Dp_{gmd} of the nucleated particles during the
352 NPF event. The measured D_{50} was lower than the recalculated D_{50} by about 10 nm. As a result, the
353 Dp_{gmd} reached the measured D_{50} at about 15:00 LT, about two hours earlier than it arrived at the
354 recalculated D_{50} , which indicates that the surfactant effects could lead to earlier activation of the newly-
355 formed particles as CCN. The earlier the Dp_{gmd} reaches the critical diameter D_{50} , the higher the N_{CCN}
356 is because more particles can survive from being scavenged by preexisting particles. The difference of
357 PNSD at the time when the Dp_{gmd} reached respectively the measured D_{50} and the recalculated D_{50} was
358 shown in Fig. 1S. The peak value of PNSD at 15:00 LT was about 20000 cm^{-3} higher than the value at
359 17:15 LT. The N_{CCN} also shows a difference (Fig. 4a).

360 We also investigate the effect of the surface tension on the N_{CCN} at SS=1.0% by varying the value



361 of the surface tension. As we mentioned in the beginning of this section, a surface tension of 0.060 N
362 m^{-1} ($\sigma_{s/a}^*$) was adopted when discussing the CCN activation at 1.0% SS and we assume that the
363 recalculated D_{50} was based on this surface tension value. The average D_{50} was the mean of the measured
364 and recalculated D_{50} . The N_{CCN} is calculated by integrating particle concentrations above D_{50} using the
365 following equation,

$$366 \quad N_{CCN} = \int_{D_{50}}^{\infty} n_i d \log D p_i \quad (14)$$

367 where n_i is the particle distribution function at $D p_i$. The D_{50} can be the measured or recalculated one.
368 It was shown that the N_{CCN} at SS=1.0% from integration of particles above the recalculated D_{50} was
369 significantly lower than that above the measured D_{50} after 12:00 LT (two hours after the occurrence of
370 the NPF event), with concentration differences of about 3000-4000 cm^{-3} (Fig. 4a). The AR based on the
371 recalculated D_{50} reached its minimal values between 10:00 and 12:00 LT, and then steadily increased
372 until 22:00 and subsequently decreased. The AR based on the measured D_{50} reached its minimal during
373 the same period as the AR from the recalculated D_{50} ; however, it then rapidly increased until 16:00 and
374 the continuing increase of the AR was much slower until 22:00, and also subsequently decrease for the
375 last hour of the measurement (Fig. 4b). This different trend was likely attributed to the continuing growth
376 of the nucleated particles to the CCN size prior to 16:00. Here, we define the deviation of N_{CCN} based on
377 the recalculated D_{50} from that based on the measured D_{50} to evaluate the impacts of the surface tension
378 (primarily due to the surfactant effects) on the N_{CCN} ,

$$379 \quad \delta_{N_{CCN}} = \frac{N_{CCN,m} - N_{CCN,r}}{N_{CCN,m}} \quad (15)$$

380 where the $N_{CCN,m}$, $N_{CCN,r}$ represent the N_{CCN} based on the measured D_{50} and the recalculated D_{50} or
381 average D_{50} . The $\delta_{N_{CCN}}$ of the recalculated D_{50} was about 0.1 prior to the NPF event, and reached a
382 peak value of 0.4 at 14:00 LT, and then decreased steadily to 0.1 at 22:00 and remained unchanged for



383 the last hour of the measurement (Fig. 4c). The results suggests that the decrease of the surface tension
384 due to the surfactant effects could lead to about 10% increase of the N_{CCN} at 1.0% SS for non-event
385 period and about 40% increase during the NPF event (Fig. 4c). Apparently, the surfactants have more
386 significant effects on N_{CCN} during the NPF event period than during non-event period, as the difference
387 between the $\delta_{N_{CCN}}$ based on the recalculated D_{50} and the average D_{50} was significant only during the
388 event period (12:00-18:00 LT).

389 The hygroscopicity of newly-formed particles can have profound impact on the N_{CCN} during the
390 NPF event. During the campaign, the minimum particle size of CCN activity measurement was about
391 40-45 nm, thus the hygroscopicity of this size range was used to present the property of newly-formed
392 particles. In general, the hygroscopic parameter κ values for particles with a size range of 40-45 nm were
393 significantly higher during the early event period than during the non-event and other event periods,
394 corresponding to much higher hygroscopicity during the early event period than during the non-event
395 and other event periods (Fig. S2a). The calculated H_2SO_4 concentration peaked at about 10:00-11:00 and
396 subsequently decreased to a low level (about $0.5 \times 10^7 \text{ cm}^{-3}$) until 16:00, implying that the increase of
397 hygroscopicity was related to the condensation of H_2SO_4 vapors. It should be pointed out that the high κ
398 values during 10:00~12:00 LT did not represent the hygroscopicity of newly-formed particles which were
399 primarily composed of particles much smaller than 30-40 nm. Those newly-formed particles grew to
400 about 40-50 nm at 14:00-16:00 (Fig.1a and Fig.3) and their κ values were obviously lower than the
401 average ones, implying that the organic vapors could play an important role during growth of newly-
402 formed particle as discussed in Section 3.1. The decrease of hygroscopicity due to condensation of
403 organic vapors can lead to an increase of about 3-4 nm for the D_{50} , much smaller than the increase of
404 about 10 nm induced by the surfactant effect which reduces the surface tension as discussed before. The



405 results indicate that the surfactant effect may play a more important role than hygroscopicity in the N_{CCN}
406 because the surfactant effect can largely decrease the D_{50} during the NPF event when the number
407 concentration of particles is dominant by Aitken mode.

408 **3.3 The impact of the dynamic processes on N_{CCN}**

409 As discussed in section 2.3.4, the dynamical processes for newly-formed particles during nucleation
410 events are governed by the population balance equation (Eq. (13)). Here, we build a MATLAB program
411 to model the NPF event using Eq. 13, with input parameters including background particle distribution,
412 growth rate and formation rate. Notice that the simulation is based on the aforementioned three
413 assumptions. Figure 5 shows the measured and modeled PNSD, N_{CN} , and N_{CCN} at 1.0% SS. To be
414 simplified, the background particle distribution was assumed to be the average particle distribution before
415 6:00 LT. The modeled PNSD and N_{CN} agree very well with the measured ones, except the model fell to
416 reproduce the abrupt change of PNSD and N_{CN} between 18:00 and 22:00. As discussed in section 3.1,
417 this discrepancy was attributed to the change of the air mass by wind direction which was not considered
418 in the model. However, there are considerable discrepancies between the modeled and the measured
419 N_{CCN} . The measured N_{CCN} at 1.0% SS increased steadily after the occurrence of the NPF event (at around
420 9:00 LT) due to formation of high concentration particles at a size range of 10-60 nm until around 19:00
421 and subsequently the N_{CCN} dropped for the rest of the day. The model N_{CCN} started to increase at about
422 14:15 LT and reached its maximum level at about 17:00 LT. The model fell to reproduce the increase of
423 the measured N_{CCN} before 16:00, although the reasons corresponding to the discrepancy are still unknown.
424 The modeled peak value of the N_{CCN} at 1.0% SS was about 12000 cm^{-3} , which agreed very well with the
425 measured one (11000 cm^{-3}). Again, the model fell to reproduce the increase of N_{CCN} due to the change of



426 the air mass between 18:00 and 22:00.

427 The effects of variation (halving or doubling) of the growth rate, formation rate, and the background
428 PNSD on the N_{CN} and N_{CCN} were investigated to test the sensitivity of those parameters. Figure 6 shows
429 the comparison of the measured N_{CN} and N_{CCN} and the modeled one based on the half or doubling of
430 each tested parameter, respectively. As can be seen from Fig. 6a, the modeled N_{CN} values based on the
431 double GR, the double formation rate and the half background PNSD were higher than the corresponding
432 measured values, respectively, and vice versa. Doubling of the formation rate lead to formation of more
433 new particles and the half background PNSD corresponds to a low coagulation loss with pre-existing
434 particles, resulting in production of more new particles in the simulation. Doubling of the GR resulted in
435 a higher concentration of particles, probably due to the significant increases of the coagulation source
436 (Fig. S3b), while small decreases for both of the coagulation sink and growth term were found (Fig. S3a
437 and Fig. S3d). Since the newly-formed particles can grow to larger sizes under a higher GR, the PNSD
438 of new particles would be broader (Fig. S4), which provides a wider “region” for the coagulation sources.
439 Doubling of the FR (J) resulted in the highest modeled N_{CN} (about 90000 cm^{-3}) among all simulated
440 cases; however, the modeled N_{CCN} based on a double J was only the second highest value (about 15000
441 cm^{-3}). The highest modeled N_{CCN} (about 25000 cm^{-3}) was found to double the GR and moreover it peaked
442 earlier at about 14:00 LT (two hours earlier than the other cases). Similarly, the highest modeled AR
443 (about 0.82) was from doubling the GR and an earlier peak time was also found (Fig. S5). The above
444 results can be attributed to the following two possible reasons: (1) Doubling of the GR made newly-
445 formed particles grow faster to the D_{50} which facilitated the survival of more particles from coagulation
446 scavenging; (2) The N_{CN} became higher by doubling the GR. If newly-formed particle grew slowly, for
447 example, the decrease of the GR to a half value would result in growth of most particles to diameters



448 below that of the D_{50} , leading to the smallest change of the N_{CCN} compared to other cases (Fig. S5). The
449 pre-existing background particles can serve as the coagulation sinks for newly-formed particles and
450 hence can prevent them from growing to the CCN sizes. For example, under the double background
451 PNSD condition, the N_{CN} reached its peak of about 38000 cm^{-3} at about 11:00 and quickly dropped
452 afterward. The newly-formed particles contributed about 3000 cm^{-3} to the N_{CCN} , or an AR of about 0.45
453 at about 17:30 LT, an insignificant change compared to the value for the non-event period, implying that
454 under a high background particle concentration, NPF events a minor contribution to the N_{CCN} . Doubling
455 or halving of the FR resulted respectively in contribution of about 11000 and 5000 cm^{-3} to the N_{CCN} ;
456 however, the magnitude of contribution from variation of the FR was relatively lower than that from the
457 GR and the background PNSD.

458 Figure 7 shows the comparison of the itemized absolute and fractional contribution of coagulation
459 sink, coagulation source, GR and J to the N_{CCN} for the above several scenarios (model, double GR, half
460 or double J, and half or double PNSD). Here, the individual contribution was integrated from the
461 corresponding term in Eq. (13) for all particle sizes from the initial time of the NPF event to the time
462 when the N_{CCN} reached the peak concentration. As clearly shown in Fig. 7, the coagulation source term
463 plays an more important role in the N_{CCN} (with a fraction of about 13%) for the double GR case than any
464 other cases. As discussed above, doubling of FR (J) and halving of PNSD led to similar N_{CCN} peak values
465 (about 15000 and 13500 cm^{-3} , respectively); however, the dynamics processes for the two scenarios were
466 significantly different. For the double J case, the formation term contributed about 240000 cm^{-3} to the
467 N_{CCN} , much higher than the half PNSD case, and the CoagSnk and CoagSrc terms were much higher
468 (about -260000 and 50000 cm^{-3} , respectively) than any other cases due to formation of high concentration
469 of newly-formed particles. Moreover, under the double J scenario, the fraction of CoagSnk term was



470 higher, while the CoagSrc term was lower than the half PNSD case, indicating a more significant
471 coagulation scavenging with preexisting particles. As a result, the N_{CN} quickly dropped from its peak
472 value to a concentration level similar to the half PNSD case within one hour (Fig. 6a). Based on the
473 above reasons, the contribution of the newly-formed particles to the N_{CCN} was relatively smaller for the
474 double J case than the double GR or half PNSD cases, although its coagulation source term and J term
475 were the highest among all the cases.

476 3.4 Modeling of the impact factors on the N_{CCN} during NPF events

477 Here we include two more NPF events to investigate the influence of several important impact
478 factors (growth rate, formation rate, and background particles) on the N_{CCN} , one from this campaign
479 (October 18th, 2019), another from the field campaign in Panyu (December 12th, 2014). Both campaigns
480 were conducted in the PRD region, details of the field campaign in Panyu can be found in Cai et al.
481 (2018). We applied the same model to simulate NPF as discussed in the previous section. Figure 8 shows
482 the measured (a), modeled (b) PNSD, along with the N_{CN} (c). For a better comparison among all the
483 cases, all the modeled PNSDs were based on the measured formation rate (J_{10}) due to lack of
484 measurement data for particles below 10 nm in the Panyu campaign. The background particle
485 distributions were assumed to be the average values before 7:00 LT. In addition, since no measurement
486 data were available for the CCN activity at 1.0% SS during the Panyu campaign, the N_{CCN} for this
487 campaign was calculated from the average CCN activation curve at 1.0% SS in the two Heshan events
488 and the PNSD of the Panyu event using following equation,

$$489 \quad N_{CCN} = \int_{Dp_i=Dp_{min}}^{\infty} AR_i n_i d \log Dp_i \quad (16)$$

490 where the AR_i is the average activation ratio (in Heshan) at Dp_i and the n_i is the particle distribution



491 function (in Panyu) at Dp_i .

492 In general, the modeled PNSDs agreed well with the measured ones for the NPF events under
493 investigation (Fig. 8a-f). The N_{CN} values were excellently predicted during the initial particle formation
494 period before the maximum values were reached (Fig. 8g-i). In particular, the N_{CN} was well predicted for
495 the study case (the October 29 event) except for the period when the air mass changed as has been
496 discussed in the previous section. For the October 18 event, however, the model began to underpredict
497 the N_{CN} shortly after the N_{CN} reached the peak value, while for the Panyu event (the December 12 event),
498 a significant underestimate (about 4100 cm^{-3} lower than the measured N_{CN}) for the peak concentration
499 was made at about 12:00 pm, due probably to the presence of a significant amount of other bigger
500 background particles (100-200 nm) after 12:00 pm which was not able to be taken into account in the
501 model (Fig. 8c). As a result, the predicted N_{CCN} value was substantially lower than the measured one for
502 the December 12 event (Fig. 9c). This also indicates that the N_{CCN} was primarily contributed from the
503 background preexisting particles rather than newly-formed particles from the NPF event in the December
504 12 event case. The maximum modeled peak N_{CCN} value (about 7000 cm^{-3}) is significantly lower than that of
505 the other two events (about 15000 and 12000 cm^{-3} , respectively), which could be attributed to the lower
506 growth rates, formation rate, and the high CS value (Fig. S6 for J_{10} and table S1 for GR and CS). We
507 further simulate the December 12 event to investigate the most important impact factor that influences
508 the N_{CCN} using different characteristics from the two other NPF events, including the growth rate on the
509 October 18 event (high growth rate scenario), the formation rate on the October 29 event (high formation
510 rate scenario) and the background PNSD on the October 29 event (mainly distributed in Aitken mode).
511 The results show that all the new modeled N_{CN} value were higher than the initial modeled N_{CN} value.
512 The N_{CN} was significantly increased and earlier peaked (with a peak value about 38000 cm^{-3}) under the



513 high formation rate scenario, while the N_{CCN} was mainly affected and also earlier peaked under the high
514 growth rate scenario. The peak value of N_{CCN} increased from 6000 cm^{-3} to 14000 cm^{-3} and the peak time
515 varied from 20:00 LT to 16:00 LT. The N_{CN} value increased under the new background scenario; however,
516 the N_{CCN} barely changed, implying that larger size particles in the preexisting background play a more
517 important role in scavenging newly-formed particles. We hence conclude that the newly-formed particles
518 with a higher growth rate would grow faster to the CCN size by avoiding higher number concentration
519 losses in the atmosphere (Fig. S7a). Our results highlight the importance of particle growth rate in
520 modulating the N_{CCN} during NPF events.

521 4 Conclusions

522 Field measurements were conducted at a rural site in the PRD region of China during October and
523 November 2019. The contribution of new particle formation (NPF) to the N_{CCN} was investigated based
524 on three chosen NPF events including two (29th October and 18th November, 2019) from this field
525 campaign and one (12th December, 2014) from a previous campaign in Panyu. The effects of several
526 controlling factors on the contribution were explored to better understand the CCN activation process.
527 These factors include formation rate, growth rate, background particle distribution, hygroscopicity and
528 surface tension of the particles. Significant discrepancies were found for the κ values between
529 measurements under supersaturation (using CCNc) and those under sub-saturation (using HTDMA), due
530 partly to the pure water assumption for the surface tension when calculating the κ values based on the
531 CCNc measurements. Organics in the particles could act as surfactants to lower the surface tension which
532 facilitate CCN activation during NPF events. The results show that a surface tension value of about 0.060
533 N m^{-1} instead of 0.073 N m^{-1} (pure water assumption) could decrease the D_{50} (SS=1.0%) for 10 nm



534 particles, bringing the agreement of the κ values between CCNc and HTDMA measurements. The
535 surfactant effects caused by organics in the particles would increase the N_{CCN} at SS=1.0% by about 20%
536 during non-event periods and by about 40% during NPF events. In addition, an earlier peak time was
537 also observed because much higher number concentrations of small particles (3-100 nm) during the event
538 would lead to smaller D_{50} .

539 The dynamic population balance equations were employed to qualitatively simulate NPF events
540 under different case scenarios (coagulation term, formation term and growth term). Sensitivity studies
541 were then performed to analyze the contribution of each aforementioned term to the N_{CCN} . The results
542 show that high formation rates, high growth rates, and low background particle concentrations lead to
543 high total and CCN concentrations, although different mechanisms were attributed to the high N_{CN} and
544 N_{CCN} . High formation rates lead to high particle production in the atmosphere; likewise, high growth
545 rates produce a broad distribution of new particles and further increase the coagulation sources, while
546 low background concentrations result in low coagulation scavenging with preexisting particles. Among
547 these controlling factors, the growth rate was found to have the most profound impact on the N_{CCN} ,
548 because a faster growth for newly-formed particles resulted in growing these particles to the CCN sizes
549 in a shorter time before they were scavenged by preexisting particles. The N_{CCN} (SS=1.0%) measured
550 from the chosen event on 12th December, 2014 was significantly lower than that from two other chosen
551 events, initially attributed to the low growth rate, low formation rate, and low background particle
552 concentration. Sensitivity tests were then performed under different scenarios (the highest growth rate
553 from the event on 18th October, the highest formation rate and the lowest CS from the event on 29th
554 October, respectively) with change of only one factor for each simulation. The results show that the peak
555 value of the modeled N_{CCN} increased from 6000 to 14000 cm^{-3} with the new applied growth rate, leading



556 to a similar value to that from the event on 18th October, while the modeled N_{CCN} values were barely
557 affected under the two other scenarios. These results highlight the importance of the growth rate in the
558 contribution of the controlling factors to the N_{CCN} . We concluded that surface tension and growth rate
559 played a major role in the contribution of NPF event to the N_{CCN} . More work on the other NPF cases is
560 obviously needed in order to better understand the contribution to the N_{CCN} and its impact on climate.

561

562 *Data availability.* Data from the measurements are available upon request (Bin Yuan via
563 byuan@jnu.edu.cn).

564

565 *Supplement.* The supplement related to this article is available online at xxx.

566

567 *Author contributions.* **MC, MS** and **BY** designed the research. **MC, MS, BY, SH, YP, ZW, BL** and **QS**
568 performed the measurements. **MC, BY, JZ, HT, FL, SH, HX, LL, YP, ZW, BL** and **QS** analyzed the
569 data. **MC, BY** and **JZ** wrote the paper with contributions from all co-authors.

570

571 *Competing interests.* The authors declare that they have no conflict of interest.

572

573 *Acknowledgements.* This work was supported by the Key-Area Research and Development Program of
574 Guangdong Province (grant No. 2019B110206001), the National Key R&D Plan of China (grant No.
575 2019YFE0106300, 2018YFC0213904), the National Natural Science Foundation of China (grant No.
576 41877302, 91644225, 41775117), Guangdong Natural Science Funds for Distinguished Young Scholar
577 (grant No. 2018B030306037), Guangdong Innovative and Entrepreneurial Research Team Program



578 (grant No. 2016ZT06N263), and Guangdong Province Key Laboratory for Climate Change and Natural
579 Disaster Studies (Grant 2020B1212060025).

580 **Reference**

581 An, J., Wang, H., Shen, L., Zhu, B., Zou, J., Gao, J., and Kang, H.: Characteristics of new particle
582 formation events in Nanjing, China: Effect of water-soluble ions, *Atmos. Environ.*, 108, 32-40,
583 <https://doi.org/10.1016/j.atmosenv.2015.01.038>, 2015.

584 Asmi, E., Frey, A., Virkkula, A., Ehn, M., Manninen, H., Timonen, H., Tolonen-Kivimäki, O.,
585 Aurela, M., Hillamo, R., and Kulmala, M.: Hygroscopicity and chemical composition of Antarctic sub-
586 micrometre aerosol particles and observations of new particle formation, *Atmos. Chem. Phys.*, 10, 4253-
587 4271, 2010.

588 Boy, M., Kulmala, M., Ruuskanen, T. M., Pihlatie, M., Reissell, A., Aalto, P. P., Keronen, P., Dal
589 Maso, M., Hellen, H., Hakola, H., Jansson, R., Hanke, M., and Arnold, F.: Sulphuric acid closure and
590 contribution to nucleation mode particle growth, *Atmos. Chem. Phys.*, 5, 863-878, 10.5194/acp-5-863-
591 2005, 2005.

592 Cai, M., Tan, H., Chan, C. K., Qin, Y., Xu, H., Li, F., Schurman, M. I., Liu, L., and Zhao, J.: The
593 size-resolved cloud condensation nuclei (CCN) activity and its prediction based on aerosol
594 hygroscopicity and composition in the Pearl Delta River (PRD) region during wintertime 2014, *Atmos.*
595 *Chem. Phys.*, 18, 16419-16437, 2018.

596 Casquero-Vera, J. A., Lyamani, H., Dada, L., Hakala, S., Paasonen, P., Román, R., Fraile, R., Petäjä,
597 T., Olmo-Reyes, F. J., and Alados-Arboledas, L.: New particle formation at urban and high-altitude
598 remote sites in the south-eastern Iberian Peninsula, *Atmos. Chem. Phys. Discuss.*, 2020, 1-32,
599 10.5194/acp-2020-394, 2020.

600 Chen, C., Hu, M., Wu, Z., Wu, Y., Guo, S., Chen, W., Luo, B., Zhang, Y., and Xie, S.:
601 Characterization of new particle formation event in the rural site of Sichuan Basin and its contribution to
602 cloud condensation nuclei, *China Environ. Sci.*, 34, 2764-2772, 2014. (in Chinese)

603 Dameto de España, C., Wonaschütz, A., Steiner, G., Rosati, B., Demattio, A., Schuh, H., and



604 Hitzenberger, R.: Long-term quantitative field study of New Particle Formation (NPF) events as a source
605 of Cloud Condensation Nuclei (CCN) in the urban background of Vienna, *Atmos. Environ.*, 164, 289-
606 298, <https://doi.org/10.1016/j.atmosenv.2017.06.001>, 2017.

607 Deng, Y., Yai, H., Fujinari, H., Kawana, K., Nakayama, T., and Mochida, M.: Diurnal variation and
608 size dependence of the hygroscopicity of organic aerosol at a forest site in Wakayama, Japan: their
609 relationship to CCN concentrations, *Atmos. Chem. Phys.*, 19, 5889-5903, [10.5194/acp-19-5889-2019](https://doi.org/10.5194/acp-19-5889-2019),
610 2019.

611 Engelhart, G., Asa-Awuku, A., Nenes, A., and Pandis, S.: CCN activity and droplet growth kinetics
612 of fresh and aged monoterpene secondary organic aerosol, *Atmos. Chem. Phys.*, 8, 3937-3949, 2008.

613 Farmer, D. K., Cappa, C. D., and Kreidenweis, S. M.: Atmospheric Processes and Their Controlling
614 Influence on Cloud Condensation Nuclei Activity, *Chemical Reviews*, 115, 4199, 2015.

615 Fuchs, N., and Sutugin, A.: High Dispersed Aerosols, *Topics in Current Aerosol Research*, in:
616 *International Reviews in Aerosol Physics and Chemistry*, Pergamon Press Oxford, 5-60, 1971.

617 Jiang, J., Zhao, J., Chen, M., Eisele, F. L., Scheckman, J., Williams, B. J., Kuang, C., and McMurry,
618 P. H.: First Measurements of Neutral Atmospheric Cluster and 1–2 nm Particle Number Size
619 Distributions During Nucleation Events, *Aerosol Sci. Technol.*, 45, ii-v, [10.1080/02786826.2010.546817](https://doi.org/10.1080/02786826.2010.546817),
620 2011.

621 Kalkavouras, P., E. Bossioli, S. Bezantakos, A. Bougiatioti, N. Kalivitis, I. Stavroulas, G.
622 Kouvarakis, A. P. Protonotariou, A. Dandou, G. Biskos, N. Mihalopoulos, A. Nenes, & M. Tombrou
623 (2017), New particle formation in the southern Aegean Sea during the Etesians: importance for CCN
624 production and cloud droplet number, *Atmos. Chem. Phys.*, 17(1), 175-192, [doi:10.5194/acp-17-175-](https://doi.org/10.5194/acp-17-175-2017)
625 2017.

626 Kuang, C., Chen, M., Zhao, J., Smith, J., McMurry, P. H., and Wang, J.: Size and time-resolved
627 growth rate measurements of 1 to 5 nm freshly formed atmospheric nuclei, *Atmos. Chem. Phys.*, 12,
628 3573-3589, [10.5194/acp-12-3573-2012](https://doi.org/10.5194/acp-12-3573-2012), 2012.

629 Kulmala, M., Vehkamäki, H., Petäjä, T., Dal Maso, M., Lauri, A., Kerminen, V. M., Birmili, W., and
630 McMurry, P. H.: Formation and growth rates of ultrafine atmospheric particles: a review of observations,
631 *J. Aerosol Sci.*, 35, 143-176, <https://doi.org/10.1016/j.jaerosci.2003.10.003>, 2004.

632 Kulmala, M., Petäjä, T., Mönkkönen, P., Koponen, I. K., Dal Maso, M., Aalto, P. P., Lehtinen, K. E.



633 J., and Kerminen, V. M.: On the growth of nucleation mode particles: source rates of condensable vapor
634 in polluted and clean environments, *Atmos. Chem. Phys.*, 5, 409-416, 10.5194/acp-5-409-2005, 2005.

635 Lehtinen, K. E. J., and Kulmala, M.: A model for particle formation and growth in the atmosphere
636 with molecular resolution in size, *Atmos. Chem. Phys.*, 3, 251-257, 10.5194/acp-3-251-2003, 2003.

637 Leng, C., Zhang, Q., Tao, J., Zhang, H., Zhang, D., Xu, C., Li, X., Kong, L., Cheng, T., and Zhang,
638 R.: Impacts of new particle formation on aerosol cloud condensation nuclei (CCN) activity in Shanghai:
639 case study, *Atmos. Chem. Phys.*, 14, 11353-11365, 2014.

640 Liu, P., Song, M., Zhao, T., Gunthe, S. S., Ham, S., He, Y., Qin, Y. M., Gong, Z., Amorim, J. C.,
641 Bertram, A. K., and Martin, S. T.: Resolving the mechanisms of hygroscopic growth and cloud
642 condensation nuclei activity for organic particulate matter, *Nat. Commun.*, 9, 4076, 10.1038/s41467-018-
643 06622-2, 2018.

644 Liu, S., Hu, M., Wu, Z., Wehner, B., Wiedensohler, A., and Cheng, Y.: Aerosol number size
645 distribution and new particle formation at a rural/coastal site in Pearl River Delta (PRD) of China, *Atmos.*
646 *Environ.*, 42, 6275-6283, 2008.

647 Liu, P. F., Zhao, C. S., Göbel, T., Hallbauer, E., Nowak, A., Ran, L., Xu, W. Y., Deng, Z. Z., Ma, N.,
648 Mildenerger, K., Henning, S., Stratmann, F., and Wiedensohler, A.: Hygroscopic properties of aerosol
649 particles at high relative humidity and their diurnal variations in the North China Plain, *Atmos. Chem.*
650 *Phys.*, 11, 3479-3494, 10.5194/acp-11-3479-2011, 2011.

651 Ma, N., Zhao, C., Tao, J., Wu, Z., Kecorius, S., Wang, Z., Größ, J., Liu, H., Bian, Y., and Kuang, Y.:
652 Variation of CCN activity during new particle formation events in the North China Plain, *Atmos. Chem.*
653 *Phys.*, 16, 8593-8607, 2016.

654 Mönkkönen, P., Koponen, I. K., Lehtinen, K. E. J., Hämeri, K., Uma, R., and Kulmala, M.:
655 Measurements in a highly polluted Asian mega city: observations of aerosol number size distribution,
656 modal parameters and nucleation events, *Atmos. Chem. Phys.*, 5, 57-66, 10.5194/acp-5-57-2005, 2005.

657 Moore, R. H., Nenes, A., and Medina, J.: Scanning Mobility CCN Analysis—A Method for Fast
658 Measurements of Size-Resolved CCN Distributions and Activation Kinetics, *Aerosol Sci. Technol.*, 44,
659 861-871, 10.1080/02786826.2010.498715, 2010.

660 Nieminen, T., Lehtinen, K. E. J., and Kulmala, M.: Sub-10 nm particle growth by vapor
661 condensation – effects of vapor molecule size and particle thermal speed, *Atmos. Chem. Phys.*, 10, 9773-



-
- 662 9779, 10.5194/acp-10-9773-2010, 2010.
- 663 Nieminen, T., Asmi, A., Dal Maso, M., Aalto, P. P., Keronen, P., Petäjä, T., Kulmala, M., and
664 Kerminen, V.-M.: Trends in atmospheric new-particle formation: 16 years of observations in a boreal-
665 forest environment, *Boreal Environ. Res.*, 19 (suppl. B):191-214, 2014.
- 666 Ovadnevaite, J., Zuend, A., Laaksonen, A., Sanchez, K. J., Roberts, G., Ceburnis, D., Decesari, S.,
667 Rinaldi, M., Hodas, N., Facchini, M. C., Seinfeld, J. H., and O' Dowd, C.: Surface tension prevails over
668 solute effect in organic-influenced cloud droplet activation, *Nature*, 546, 637-641, 10.1038/nature22806,
669 2017.
- 670 Paasonen, P., Nieminen, T., Asmi, E., Manninen, H. E., Petäjä, T., Plass-Dülmer, C., Flentje, H.,
671 Birmili, W., Wiedensohler, A., Hörrak, U., Metzger, A., Hamed, A., Laaksonen, A., Facchini, M. C.,
672 Kerminen, V. M., and Kulmala, M.: On the roles of sulphuric acid and low-volatility organic vapours in
673 the initial steps of atmospheric new particle formation, *Atmos. Chem. Phys.*, 10, 11223-11242,
674 10.5194/acp-10-11223-2010, 2010.
- 675 Pajunoja, A., Lambe, A. T., Hakala, J., Rastak, N., Cummings, M. J., Brogan, J. F., Hao, L.,
676 Paramonov, M., Hong, J., and Prisle, N. L.: Adsorptive uptake of water by semisolid secondary organic
677 aerosols, *Geophys. Res. Lett.*, 42, 3063-3068, 2015.
- 678 Petäjä, T., Mauldin Iii, R., Kosciuch, E., McGrath, J., Nieminen, T., Paasonen, P., Boy, M., Adamov,
679 A., Kotiaho, T., and Kulmala, M.: Sulfuric acid and OH concentrations in a boreal forest site, *Atmos.*
680 *Chem. Phys.*, 9, 7435-7448, 2009.
- 681 Petters, M., and Kreidenweis, S.: A single parameter representation of hygroscopic growth and cloud
682 condensation nucleus activity, *Atmos. Chem. Phys.*, 7, 1961-1971, 2007.
- 683 Rastak, N., A. Pajunoja, J. C. Acosta Navarro, J. Ma, M. Song, D. G. Partridge, A. Kirkevåg, Y.
684 Leong, W. W. Hu, N. F. Taylor, A. Lambe, K. Cerully, A. Bougiatioti, P. Liu, R. Krejci, T. Petäjä, C.
685 Percival, P. Davidovits, D. R. Worsnop, A. M. L. Ekman, A. Nenes, S. Martin, J. L. Jimenez, D. R. Collins,
686 D. O. Topping, A. K. Bertram, A. Zuend, A. Virtanen, & I. Riipinen (2017), Microphysical explanation
687 of the RH-dependent water affinity of biogenic organic aerosol and its importance for climate, *Geophys.*
688 *Res. Lett.*, 44(10), 5167-5177, doi:10.1002/2017GL073056. Rose, C., K. Sellegri, I. Moreno, F. Velarde,
689 M. Ramonet, K. Weinhold, R. Krejci, M. Andrade, A. Wiedensohler, P. Ginot, & P. Laj (2017), CCN
690 production by new particle formation in the free troposphere, *Atmos. Chem. Phys.*, 17(2), 1529-1541,



-
- 691 doi:10.5194/acp-17-1529-2017.
- 692 Shen, L., H. Wang, Y. Yin, J. Chen, & K. Chen (2019), Observation of atmospheric new particle
693 growth events at the summit of mountain Tai (1534 m) in Central East China, *Atmos. Environ.*, 201, 148-
694 157, doi:https://doi.org/10.1016/j.atmosenv.2018.12.051.
- 695 Shen, X. J., J. Y. Sun, Y. M. Zhang, B. Wehner, A. Nowak, T. Tuch, X. C. Zhang, T. T. Wang, H. G.
696 Zhou, X. L. Zhang, F. Dong, W. Birmili, & A. Wiedensohler (2011), First long-term study of particle
697 number size distributions and new particle formation events of regional aerosol in the North China Plain,
698 *Atmos. Chem. Phys.*, 11(4), 1565-1580, doi:10.5194/acp-11-1565-2011.
- 699 Spracklen, D. V., Carslaw, K. S., Kulmala, M., Kerminen, V. M., Sihto, S. L., Riipinen, I., Merikanto,
700 J., Mann, G. W., Chipperfield, M. P., and Wiedensohler, A.: Contribution of particle formation to global
701 cloud condensation nuclei concentrations, *J. Geophys. Res. Lett.*, 35, 2008.
- 702 Stocker, D. Q.: Climate change 2013: The physical science basis, Working Group I Contribution to
703 the Fifth Assessment Report of the Intergovernmental Panel on Climate Change, Summary for
704 Policymakers, IPCC, 2013.
- 705 Stolzenburg, M. R., and McMurry, P. H.: Equations Governing Single and Tandem DMA
706 Configurations and a New Lognormal Approximation to the Transfer Function, *Aerosol Sci. Technol.*,
707 42, 421-432, 10.1080/02786820802157823, 2008.
- 708 Tan, H., Xu, H., Wan, Q., Li, F., Deng, X., Chan, P. W., Xia, D., and Yin, Y.: Design and Application
709 of an Unattended Multifunctional H-TDMA System, *J. Atmos. Oceanic Technol.*, 30, 1136-1148,
710 10.1175/JTECH-D-12-00129.1, 2013.
- 711 Vignati, E., Wilson, J., and Stier, P.: M7: An efficient size-resolved aerosol microphysics module
712 for large-scale aerosol transport models, *J. Geophys. Res. Lett.*, 109, 10.1029/2003jd004485, 2004.
- 713 Wang, S., Peng, Y., Qi, J., Wu, C., Wang, C., Wang, B., Wang, Z., Kuang, Y., Song, W., Wang, X.,
714 Hu, W., Chen, W., Shen, J., Chen, D., Shao, M., and Yuan, B.: Different chemical removal pathways of
715 volatile organic compounds (VOCs) s: Comparison of urban and regional sites, *Acta Sci. Circumst.*, 40,
716 2311-2322, 2020. (in Chinese)
- 717 Wang, X., Jin, Y. G., Suto, M., Lee, L. C., and O'Neal, H. E.: Rate constant of the gas phase reaction
718 of SO₃ with H₂O, *J. Chem. Phys.*, 89, 4853-4860, 10.1063/1.455680, 1988.
- 719 Wang, Z., Hu, M., Yue, D., He, L., Huang, X., Yang, Q., Zheng, J., Zhang, R., and Zhang, Y.: New



720 particle formation in the presence of a strong biomass burning episode at a downwind rural site in PRD,
721 China, *Tellus B: Chem. Phys. Meteor.*, 65, 19965, 10.3402/tellusb.v65i0.19965, 2013.

722 Wex, H., M. D. Petters, C. M. Carrico, E. Hallbauer, A. Massling, G. R. McMeeking, L. Poulain, Z.
723 Wu, S. M. Kreidenweis, & F. Stratmann (2009), Towards closing the gap between hygroscopic growth
724 and activation for secondary organic aerosol: Part 1 – Evidence from measurements, *Atmos. Chem. Phys.*,
725 9(12), 3987-3997, doi:10.5194/acp-9-3987-2009.

726 Wolfe, G. M., Marvin, M. R., Roberts, S. J., Travis, K. R., and Liao, J.: The Framework for 0-D
727 Atmospheric Modeling (F0AM) v3.1, *Geosci. Model Dev.*, 9, 3309-3319, 10.5194/gmd-9-3309-2016,
728 2016.

729 Wu, Z., Hu, M., Liu, S., Wehner, B., Bauer, S., Maßling, A., Wiedensohler, A., Petäjä, T., Dal Maso,
730 M., and Kulmala, M.: New particle formation in Beijing, China: Statistical analysis of a 1-year data set,
731 *J. Geophys. Res.*, 112, D09209, 10.1029/2006jd007406, 2007.

732 Wu, Z., Birmili, W., Poulain, L., Wang, Z., Merkel, M., Fahlbusch, B., Pinxteren, D. v., Herrmann,
733 H., and Wiedensohler, A.: Particle hygroscopicity during atmospheric new particle formation events:
734 implications for the chemical species contributing to particle growth, *Atmos. Chem. Phys.*, 13, 6637-
735 6646, 2013a.

736 Wu, Z., Poulain, L., Henning, S., and Dieckmann, K.: Relating particle hygroscopicity and CCN
737 activity to chemical composition during the HCCT-2010 field campaign, *Atmos. Chem. Phys.*, 13, 7983-
738 7996, 2013b.

739 Yu, H., Ortega, J., Smith, J. N., Guenther, A. B., Kanawade, V. P., You, Y., Liu, Y., Hosman, K., Karl,
740 T., Seco, R., Geron, C., Pallardy, S. G., Gu, L., Mikkilä, J., and Lee, S.-H.: New Particle Formation and
741 Growth in an Isoprene-Dominated Ozark Forest: From Sub-5 nm to CCN-Active Sizes, *Aerosol Sci.*
742 *Technol.*, 48, 1285-1298, 10.1080/02786826.2014.984801, 2014.

743 Yue, D., Zhong, L., Zhang, T., Shen, J., Yuan, L., Ye, S., Zhou, Y., and Zeng, L.: Particle growth and
744 variation of cloud condensation nucleus activity on polluted days with new particle formation: A case
745 study for regional air pollution in the PRD region, China, *Aerosol Air Qual. Res.*, 16, 323-335, 2016.

746 Yue, D. L., Hu, M., Zhang, R. Y., Wu, Z. J., Su, H., Wang, Z. B., Peng, J. F., He, L. Y., Huang, X.
747 F., Gong, Y. G., and Wiedensohler, A.: Potential contribution of new particle formation to cloud
748 condensation nuclei in Beijing, *Atmos. Environ.*, 45, 6070-6077,



749 <https://doi.org/10.1016/j.atmosenv.2011.07.037>, 2011.

750 Yue, D. L., Hu, M., Wang, Z. B., Wen, M. T., Guo, S., Zhong, L. J., Wiedensohler, A., and Zhang,

751 Y. H.: Comparison of particle number size distributions and new particle formation between the urban

752 and rural sites in the PRD region, China, Atmos. Environ., 76, 181-188,

753 <https://doi.org/10.1016/j.atmosenv.2012.11.018>, 2013.

754



755 FIGURE CAPTIONS

756 Figure 1. The PNSD (a), N_{CN} , N_{CCN} and AR (b), wind speed and wind direction (c), $j_{O(1D)}$, and
757 concentration of calculated H_2SO_4 (d) during the NPF event on 29th October, 2019. The blue dots in (a)
758 represents the geometric mean particle diameter ($D_{p_{gmd}}$) and the red line represents the linear fitting.

759 Figure 2. The median and interquartile κ obtained from HTDMA and CCN measurements during this
760 campaign, at the Panyu site (urban Guangzhou), and from South China Sea. The κ was pointed against
761 the corresponding median D_{50} (CCN measurement) or selected diameter (HTDMA measurement). Dots
762 represent the median values and bars represent the interquartile ranges. The κ values in this measurement
763 were obtained from HTDMA measurement (in blue) and CCNc measurement ($ss=0.1\%$, 0.2% , 0.4% ,
764 0.7% , 0.9% , and 1.0% in red and yellow for different surface tensions). The yellow lines and dots
765 represent the κ values recalculated based on $\sigma^{s/a*}$. The κ values in the Panyu measurement were obtained
766 from HTDMA measurement (in purple) and CCNc measurement ($ss=0.1\%$, 0.2% , 0.4% , and 0.7% , in
767 green). The κ values from the South China Sea were obtained from CCNc measurement ($ss=0.18\%$,
768 0.34% , and 0.59% , in light blue). The κ values from the North China Plain were obtained from HTDMA
769 measurement.

770 Figure 3. The variation of $D_{p_{gmd}}$ (blue dots), measured D_{50} (yellow dots) and recalculated D_{50} (red dots)
771 based on pure water surface tension.

772 Figure 4. The variation of N_{CCN} (a), activation ratio (b), and δ_{CCN} (c) based on the measured D_{50} , the
773 recalculated D_{50} , and the average D_{50} . The red line represents the measured values. The yellow line
774 represents the values calculated based on the surface tension of pure water (0.072 N m^{-1}). The purple line
775 represents the values calculated from the average D_{50} . The green region represents the interquartile values
776 calculated from the interquartile D_{50} .



777 Figure. 5 The measured and model PNSD (a and b), N_{CN} (c) and N_{CCN} (c). The blue lines in (c) represent
778 the measured values and the red lines represent the model values.

779 Figure 6. The variation of measured and model N_{CN} (a) and N_{CCN} (b) at 1.0% SS. The simulations was
780 based on standard characteristic (red solid line), halving of GR, formation rate and background particle
781 distribution (orange, purple and green solid line, respectively) and doubling of GR, formation rate and
782 background particle distribution (orange, purple and green dash line, respectively).

783 Figure 7. The number contribution (a) and its fraction (b) of CoagSnk term, CoagSrc term, GR term, and
784 formation (J) term to the N_{CCN} when it reached its peak value based under different case scenarios.

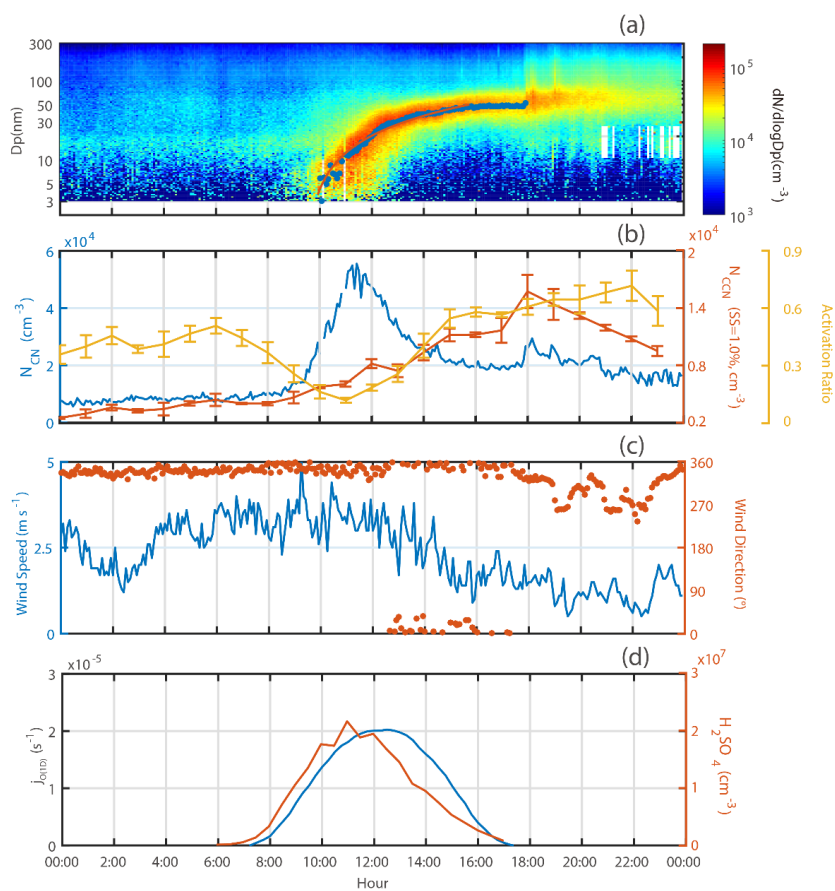
785 Figure 8. The measured PNSD (a, b, and c), model PNSD (d, e, and f), measured N_{CN} and model N_{CN} (g,
786 h, and i) during different NPF events. Solid and dash lines represent the measured and model N_{CN} ,
787 respectively.

788 Figure 9. The measured and model N_{CCN} (SS=1.0%) during different NPF events.

789 Figure 10. The measured and model N_{CN} (a) and N_{CCN} (b) on the Panyu NPF event. The blue line
790 represents the measured value. The red, yellow, purple and green lines represent the simulated N_{CCN}
791 based on standard input, growth rate of the NPF event on October 18th, formation rate of the NPF event
792 on October 29th, and new background particle distribution of the NPF event on October 29th, respectively.
793



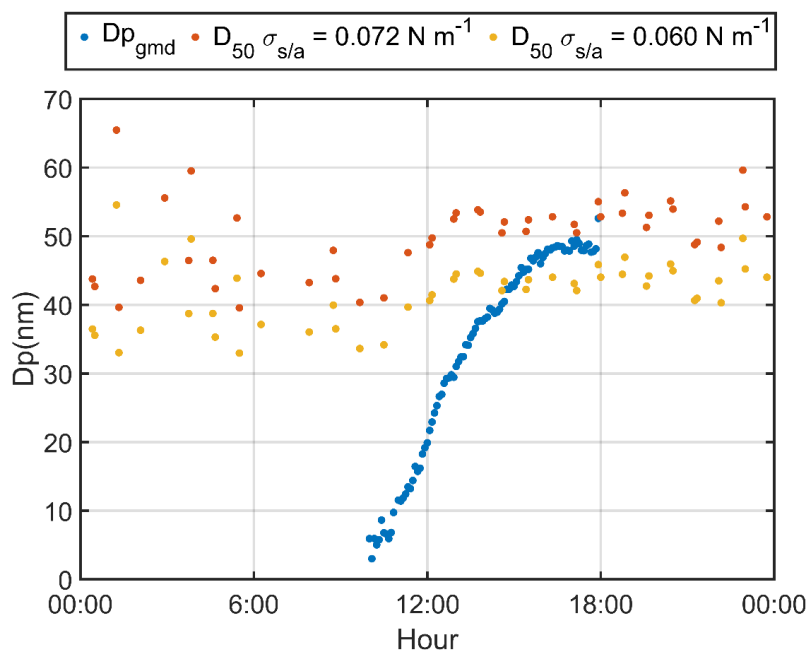
794



795

796 Fig. 1.

797

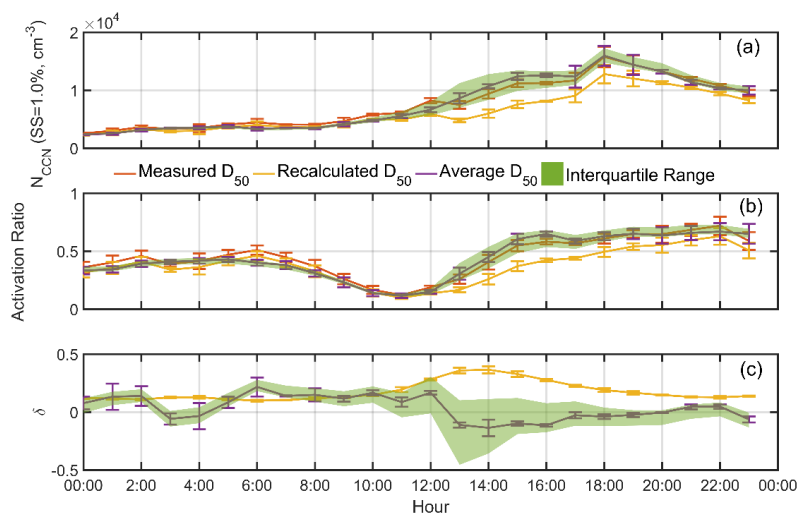


801

802

803 Fig. 3.

804

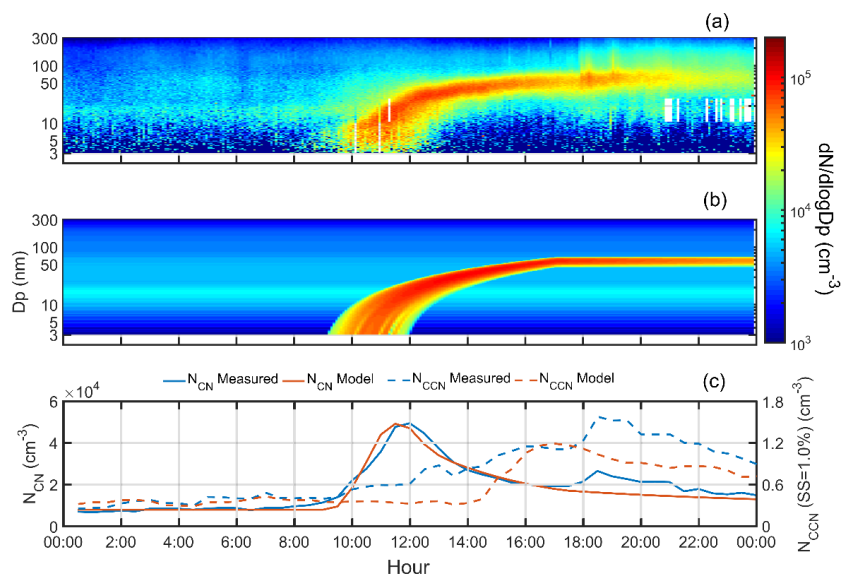


805

806

807 Fig. 4.

808

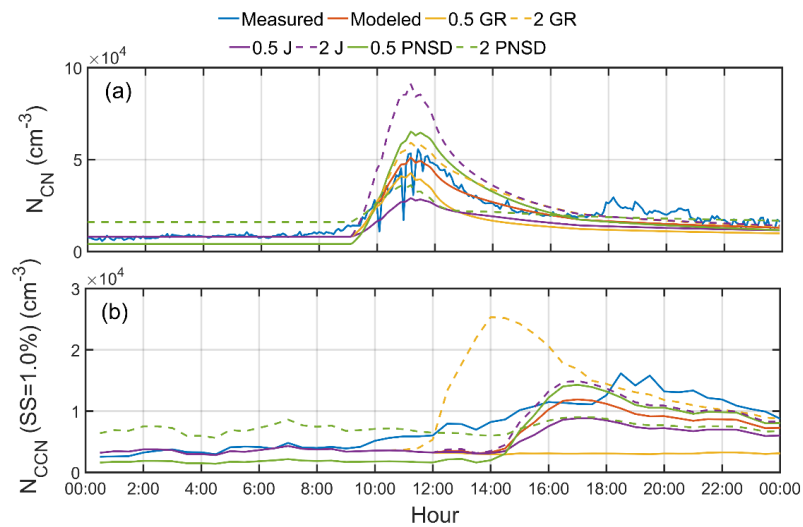


809

810

811 Fig. 5.

812

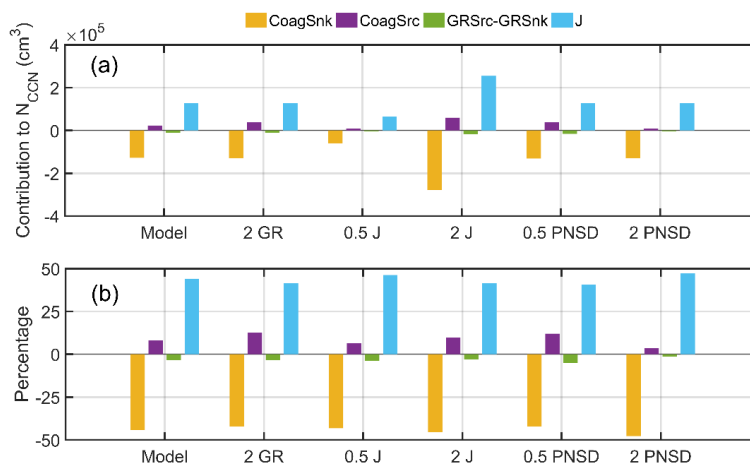


813

814

815 Fig. 6.

816

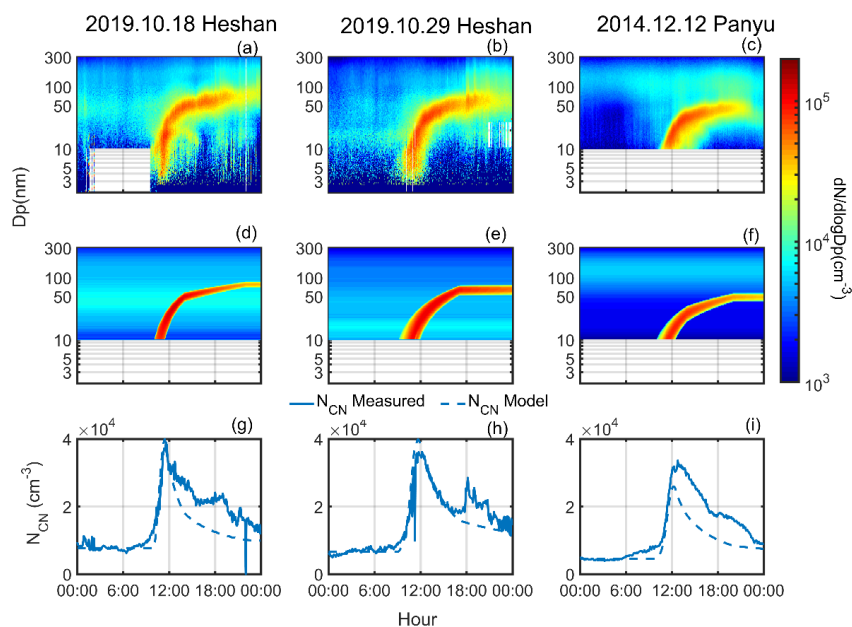


817

818

819 Fig. 7.

820

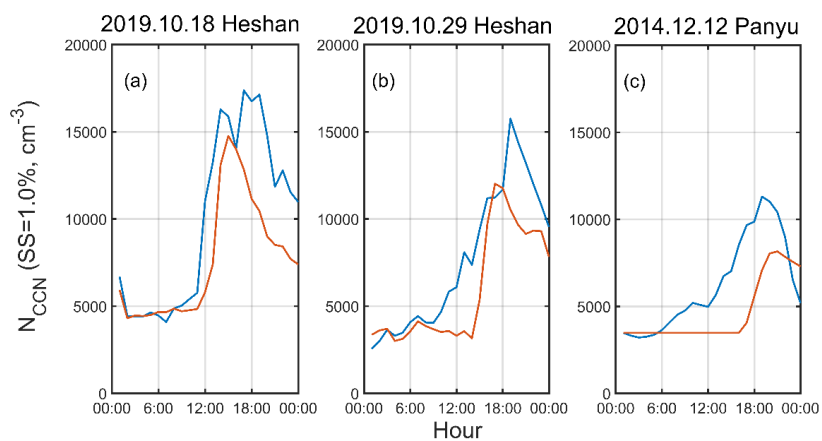


821

822

823 Fig. 8.

824

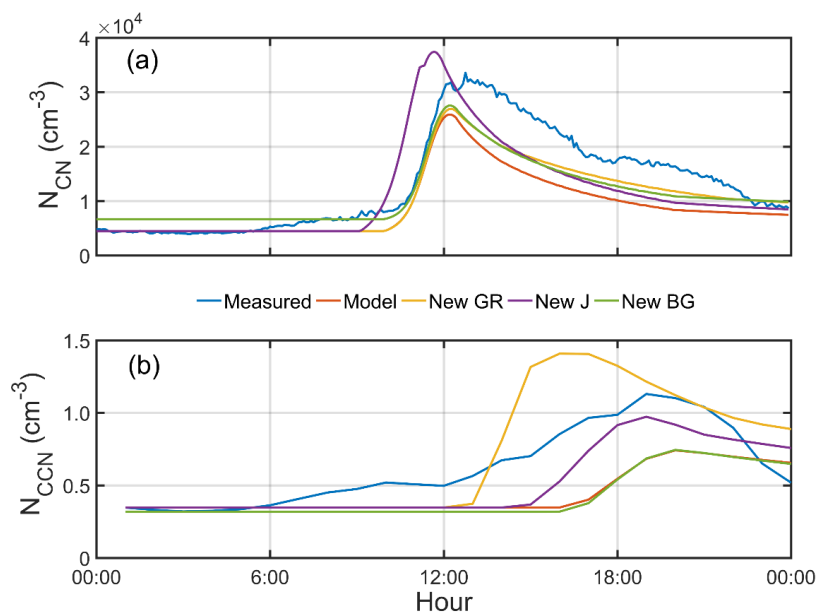


825

826

827 Fig. 9.

828



829

830

831 Fig. 10.

832

833